Basin-Width Dependence of Northern Deep Convection

Madeleine K. Youngs [1,2], Raffaele Ferrari [1], Glenn R. Flierl [1]

[1]Massachusetts Institute of Technology
[2]Woods Hole Oceanographic Institution

Key Points:

- This study illustrates that basin size favors deep convection in the North Atlantic over the North Pacific.
- A simple analytical model shows that convection shuts off for a weaker freshwater forcing per unit area in a wide basin compared to a narrow basin.
- Single-basin simulations with an ocean circulation model corroborate the prediction of the analytical model.

Corresponding author: Madeleine K. Youngs, myoungs@mit.edu

Abstract

Convection penetrates to the ocean bottom in the North Atlantic, but not in the North Pacific. This study examines the role of basin width in shutting down high-latitude ocean convection. Deep convection is triggered by polar cooling but it is opposed by precipitation. A two-layer analytical model illustrates that the overturning circulation acts to mitigate the effect of precipitation by advecting salty, dense water from subtropical latitudes to polar latitudes. the nonlinear dependence of the overturning strength on basin width makes it more efficient in a narrow basin, resulting in a convection shut-down at a stronger freshwater forcing. These predictions are confirmed by simulations with a general circulation model configured with a single closed basin to the north and a re-entrant channel to the south. This suggests that basin width may play a role in suppressing convection in the North Pacific but not in the North Atlantic.

1 Introduction

The paleo record suggests that deep convection in the North Atlantic turned on and off many times over the last few million years resulting in major climate shifts (e.g., Boyle, 1990; Thornalley, Barker, Broecker, Elderfield, & McCave, 2011). For example, the shut down of deep convection is believed to have triggered the cold Heinrich events, while the turning on of deep convection would have promoted the rapidly warming Dansgaard-Oeschger events (e.g., Loving & Vallis, 2005; Timmermann, Gildor, Schulz, & Tziperman, 2003; Walin, 1985). There is also speculation that convection may shut off again in a future warmer climate (e.g., Rahmstorf et al., 2015; Sgubin, Swingedouw, Drijfhout, Mary, & Bennabi, 2017). Accordingly, understanding what controls high latitude convection is key to a complete theory of past, present, and future climate.

Explanations for why convection occurs in the North Atlantic but not in the North Pacific have focused on the different roles of heat and salt on the overturning (Ferreira et al., 2018, and references therein). Ferreira, Marshall, and Campin (2010) pointed to the larger freshwater flux received by the North Pacific Ocean because of its larger width compared to the North Atlantic Ocean. Jones and Cessi (2017) highlighted the importance of Northern Hemisphere wind-driven gyres (and their width dependence) on the salt budget and overturning state of each basin. A few studies (Jones & Cessi, 2016; Nilsson, Langen, Ferreira, & Marshall, 2013; Weijer, de Ruijter, Dijkstra, & Van Leeuwen, 1999) contended that the inter-basin transport of salt between the Atlantic and Indo-

Pacific basins accounts for the difference in overturning states. Here we wish to demonstrate that in addition, and independently of these mechanisms, the different width (longitudinal extent) of the North Atlantic and North Pacific basins also favors convection in the narrow basin through its impact on the overturning. Our goal is not to identify which among the proposed mechanisms is most important in any specific climate. Rather we derive a scaling law to estimate the impact of freshwater fluxes on high latitude convection building on recent advances in the theory of the global overturning circulation and stratification (e.g., de Boer & Hogg, 2014; Gnanadesikan, 1999; Gnanadesikan, Kelson, & Sten, 2018; Nikurashin & Vallis, 2011, 2012; Shakespeare & Hogg, 2012). Our hope is that this scaling can then be used together with those proposed for inter-basin and gyre freshwater transports to quantify the relative importance of each process in more realistic simulations of the global ocean circulation.

We approach this problem by extending the two-layer model of Gnanadesikan (1999) to account for the different boundary conditions for temperature and salinity (restoring for the former and flux for the latter), which are believed to be crucial in selecting whether deep convection develops in the North Atlantic (e.g. Johnson, Marshall, & Sproson, 2007; Marotzke, Welander, & Willebrand, 1988; Stommel, 1961). We then examine the dependence of overturning and convection shut-off on the width of the basin in both the two-layer analytical model in section 2 and in a full primitive equation model with idealized geometry in section 3. We discuss and conclude in section 4.

2 Two-layer Analytical Model

We set up a conceptual model of the ocean overturning circulation to understand salt's role in deep convection by extending the approach of Gnanadesikan (1999). We consider a model consisting of two layers, a thermocline layer (layer t) of depth h and a deep layer (layer d), a setup similar to that used by Johnson et al. (2007) and sketched in Figure 1. Each layer has a uniform temperature and salinity given by T_t, S_t and T_d, S_d, respectively. There is a positive area-integrated freshwater flux $\mathcal{P}$ m^3 s^{-1} into the deep layer, acting to freshen it, and a surface freshwater flux of $-\mathcal{P}$ m^3 s^{-1} out of the thermocline layer, acting to make it saltier. The temperatures T_t, T_d are fixed to constant values and $T_t > T_d$. These choices are made to capture the asymmetry in surface forcing of salt and heat: a freshwater flux for salinity and a restoring to the prescribed atmospheric value for temperature (Haney, 1971).

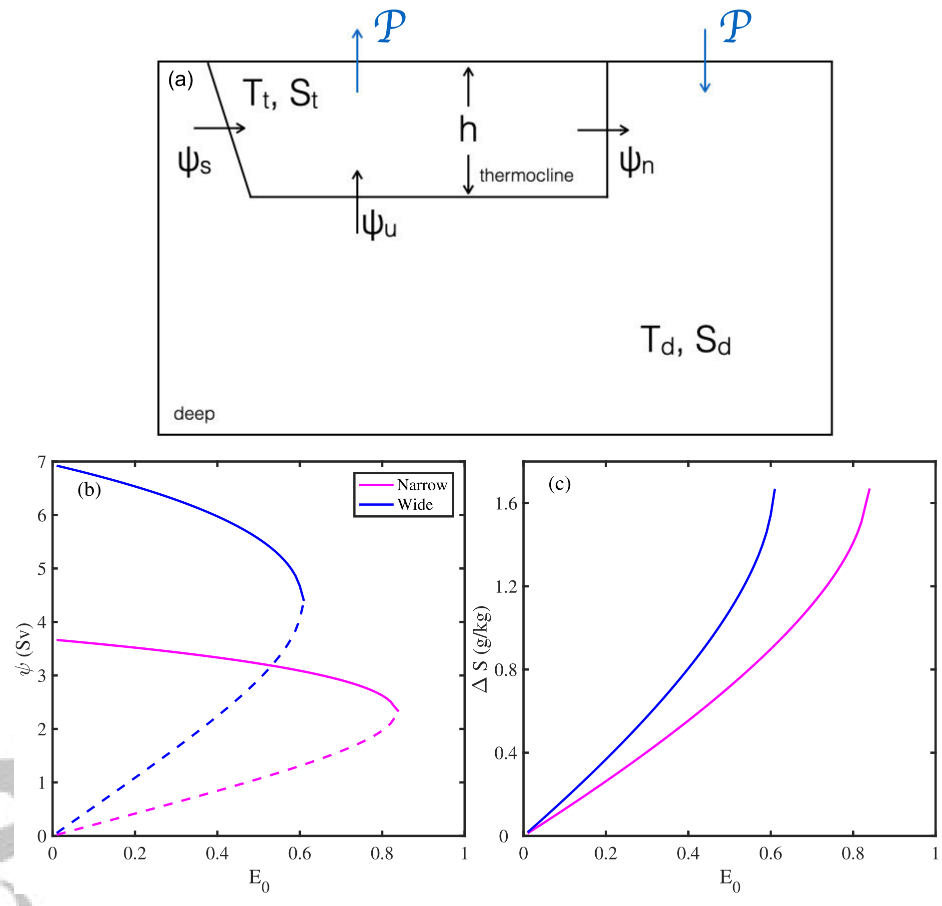

Figure 1. (a) Schematic of the conceptual model configuration. The ocean is divided in two layers of uniform temperature and salinity: a thermocline layer and a deep layer. A freshwater flux of $\mathcal{P}$ m^3 s^{-1} reduces salinity in the deep layer and an equal and opposite freshwater flux increases salinity in the thermocline layer, representing the dominance of precipitation at high latitudes and of evaporation at low latitudes. There are transports between the two layers: ψ_n represents convection which converts light to dense water, ψ_u represents the reverse conversion through deep ocean mixing and ψ_s through meridional surface flows in a "Southern Ocean". (b) ψ_n as a function of freshwater forcing, with the solid lines as the stable solutions, and dashed lines as the unstable solutions. (c) The difference in salinity between the deep and the thermocline layers as a function of freshwater forcing.

The transport of waters from the thermocline to the deep layer by deep convection is represented by ψ_n, the diffusive diabatic upwelling from the deep layer to the thermocline is represented by ψ_u, and the upwelling from the deep layer to the thermocline layer though a southern re-entrant channel is given by ψ_s, following a scaling meant to capture the dynamics of the Southern Ocean. At equilibrium the mass budget for the model requires that $\psi_n = \psi_s + \psi_u$.

2.1 Scalings for Overturning

The sinking of waters associated with deep convection in the northern hemisphere is assumed to follow the scaling first proposed by Gnanadesikan (1999),

$$\psi_n = \frac{\Delta b h^2}{f} \tag{1}$$

where Δb is the difference in buoyancy between the thermocline and the deep layer, h is the depth of the thermocline layer, and f is the high latitude Coriolis parameter. In this analytical model, $\Delta b = g(\alpha(T_t - T_d) - \beta(S_t - S_d)) = g(\alpha\Delta T - \beta\Delta S)$ where α is the thermal expansion coefficient and β is the saline contraction coefficient, $\Delta T = T_t - T_d$ and $\Delta S = S_t - S_d$ (both positive values).

The diabatic, diffusive upwelling is expressed as,

$$\psi_u = \frac{\kappa_v}{h} A \tag{2}$$

where κ_v is the vertical diffusivity, and A is the total area of the basin where upwelling occurs (Munk, 1966; Nikurashin & Vallis, 2012). This scaling represents a vertical advective-diffusive balance for buoyancy in the ocean interior. We keep the area of diffusive upwelling general in order to connect our scalings to the present day ocean where upwelling happens primarily in the Indo-Pacific and not in the convecting basin (Ferrari, Nadeau, Marshall, Allison, & Johnson, 2017; Forget & Ferreira, 2019; Holmes et al., 2019; Newsom & Thompson, 2018).

The adiabatic upwelling in a southern channel is given by the residual between Ekman transport acting to steepen isopycnals and eddies acting to relax them (Gnanadesikan, 1999; D. Marshall, 1997; J. Marshall & Radko, 2003),

$$\psi_s = \left(\frac{\tau}{\rho_0 f} - K_e \frac{h}{\ell} \right) L_x \tag{3}$$

where τ is the wind stress blowing over the channel, ρ_0 is a reference density, K_e is the Gent-McWilliams eddy diffusivity, and h/ℓ is the slope of the density surface outcropping in the southern channel (ℓ is the meridional extent of the slumping isopycnal in Fig. 1).

Two limits are potentially relevant for the ocean circulation: a diabatic limit where the northern convection deep waters are transformed back into thermocline waters through diabatic upwelling in the basin i.e. $\psi_n \simeq \psi_u$, and an adiabatic limit where the northern convection deep waters upwell adiabatically to the surface in the southern channel where they are transformed back into thermocline waters through surface heat fluxes i.e. $\psi_n \simeq \psi_s$. We will focus our analysis to the diabatic limit which is mathematically simpler. However, as we point out below, the adiabatic limit results in a qualitatively similar dependence of the overturning circulation on basin width, which is the key ingredient to explain why convection is favored in a narrower basin like the Atlantic. It is reassuring that the overturning displays the same qualitative dependence on basin width in both limits, because the numerical simulations described below and likely the real ocean are in a regime in between the two limits.

In the diabatic limit, $\psi_n = \psi_u = \psi$, and we can equate Eq. (1) and Eq. (2),

$$\frac{\Delta b h^2}{f} = \frac{\kappa_v}{h} A$$

and solve for h,

$$h = \left(\frac{f \kappa_v A}{\Delta b}\right)^{1/3}.$$

Substituting h back into Eq. (1) or (2) gives a scaling for the overturning,

$$\psi = \frac{\Delta b^{1/3} (\kappa_v A)^{2/3}}{f^{1/3}}. \tag{4}$$

This relationship cannot be solved for ψ, because the buoyancy difference Δb depends on the salinity difference which in turns depends on the strength of the overturning circulation as we show next.

2.2 Salt Budget

The temperature difference ΔT between the two layers is fixed, because ocean temperatures are quickly restored to the overlying atmospheric value (Haney, 1971). The salinity difference is instead the result of a balance between the air-sea freshwater flux and the salt exchange between the two layers,

$$\begin{aligned} \frac{\partial S_t V_t}{\partial t} &= \mathcal{P} S_0 + \psi (S_d - S_t) \\ \frac{\partial S_d V_d}{\partial t} &= -\mathcal{P} S_0 + \psi (S_t - S_d) \end{aligned}$$

where S_0 is a reference salinity, $\mathcal{P}$ is a positive area-integrated freshwater flux in m^3 s^{-1}. $S_0 \mathcal{P}$ is the virtual salt flux and it is equal and opposite in the two layers. V_t, V_d are the volumes of the thermocline and deep layers. Steady state solutions are obtained subtracting the two expressions and remembering that $\Delta S = S_t - S_d$ to find

$$\Delta S = \frac{\mathcal{P}}{\psi} S_0. \tag{5}$$

The salinity difference ΔS is positive ($\mathcal{P}$, S_0 and ψ are all defined positive) because evaporation over the thermocline keeps its salinity higher than that of the deep waters. This tendency is offset by the overturning ψ which acts to reduce ΔS. The freshwater flux $\mathcal{P}$ and the overturning ψ do not scale in the same way with basin size, as we discuss next. Thus the salinity difference ΔS (and thus the buoyancy difference Δb) between thermocline and deep waters will depend on basin size. Since Δb sets the strength of the sinking at high latitudes, this further implies that the strength of convection depends on basin size. This is the fundamental insight of our study.

The freshwater flux per unit area is comparable in the North Atlantic and North Pacific (Forget et al., 2015). Given that we focus on the impact of the basin width–the major geometrical difference between the North Pacific and North Atlantic–we keep the basin length fixed and write the net freshwater flux as $\mathcal{P} = E_0 L_x p$, where p is the freshwater flux per unit zonal length in m^2 s^{-1}, L_x is the basin width and E_0 is a dimensionless variable scaling factor that we use to vary the overall magnitude of the freshwater forcing. $E_0 = 1$ represents present day levels of freshwater fluxes.

2.3 Overturning Shut-off

Consistent with previous analytical and climate model studies (e.g., Dijkstra, 2007; Gnanadesikan et al., 2018; Johnson et al., 2007; Rahmstorf, 1996), our model predicts that convection shuts down when the freshwater flux exceeds a critical threshold value. This is demonstrated by substituting the expression for ΔS, equation (5), in the expression for ψ, equation (1). We obtain an expression for ψ that contains only independent parameters.

$$\psi = \frac{g^{1/3}(\alpha\Delta T - \beta E_0 L_x p S_0/\psi)^{1/3}(\kappa_v A)^{2/3}}{f^{1/3}}. \tag{6}$$

This expression can be converted into a quartic equation and the roots found. A plot ψ as a function of E_0 for two different values of basin width is shown in Fig 1b for $L_x = 3.7 \times 10^6$ m (narrow basin) and $L_x = 9.6 \times 10^6$ m (wide basin, 2.6 times wider than the narrow basin). The other parameters are set to $g = 9.8$ m s^{-2}, $\alpha\Delta T = 1 \times 10^{-3}$, $\beta = 4.5 \times 10^{-4}$kg g^{-1}, $\kappa_v = 1.2 \times 10^{-5}$ m^2 s^{-1}, $S_0 = 35$ g kg^{-1}, $f = 1 \times 10^{-4}$

s $^{-1}$, and $p = 0.0357$ m^{2}s^{-1}. For simplicity we now consider a single basin geometry and thus set $A = L_x L_y$ with $L_y = 1.6 \times 10^7$ m. A solution with $\psi > 0$, and thus convective sinking, exists only for E_0 smaller than a critical value E_{0crit} as shown in Fig. 1b. Furthermore the critical freshwater forcing E_{0crit} is larger in the narrow basin ($E_{0crit} = 0.84$) than in the wide basin ($E_{0crit} = 0.61$).

We can calculate an analytical expression for E_{0crit} by noticing that at E_{0crit}, $dE_0/d\psi = 0$. Some algebra gives,

$$E_{0crit} = \frac{3}{4^{4/3}p}\frac{(\alpha\Delta T)^{4/3}g^{1/3}(\kappa_v A)^{2/3}}{\beta f^{1/3}L_x S_0}. \tag{7}$$

The key result here is that E_{0crit} scales inversely with basin width. In the one basin model solved numerically $A = L_x L_y$ and thus $E_{0crit} \propto L_x^{-1/3}$, while in a more general situation where the upwelling happens in a different basin than the convecting one then A is fixed and $E_{0crit} \propto L_x^{-1}$. In either case convection shuts off for a weaker freshwater forcing in a wider basin.

In our model convection shuts off through a "saddle node bifurcation": for $E_0 < E_{0crit}$, there are two real roots (and a complex pair). For $E_0 > E_{0crit}$, there are no purely real roots (two complex pairs instead).

2.4 Adiabatic limit

It is straightforward to repeat the above analysis for the adiabatic limit, i.e. when $\psi_n = \psi_s$. Nikurashin and Vallis (2012) derive the expression for ψ in this limit. Following the same steps as above, one can compute the bifurcation diagram for ψ as a function of E_0. Much like in the diabatic limit, the wider basin has a smaller E_{0crit} than the narrow basin, but the dependence on L_x is weaker than in the diabatic limit. Since a wider basin has a smaller critical freshwater forcing in both the diabatic and adiabatic limits, we expect this result to hold in between the two limits as well.

3 Primitive Equations Model

3.1 Configuration

To lend credence to the analytical model, we run simulations with a full primitive equation model. We do not expect the primitive equation solutions to behave exactly like the analytical model, but do anticipate the same qualitative behavior. We use the

MITgcm in a 2° horizontal resolution configuration with a northern basin and a re-entrant channel in the south shown in Fig. 2 (J. Marshall, Adcroft, Hill, Perelman, & Heisey, 1997). We use 40 vertical layers ranging from 37 m thick at the surface to 159 m thick at the bottom. We perform single-basin experiments to test the impact of basin width on the overturning, with spherical sectors of width $L_x = 56°$ for the narrow basin, giving a basin area close to that of the Atlantic Ocean, and $L_x = 148°$ for the wider basin, giving a basin area close to that of the Indo-Pacific Ocean, 2.6 times wider than the narrow basin. The latitudinal extent of the model is 70° S to 70° N. A Scotia Arc-like ridge is placed in the southern channel and shown in Figure 2 to provide a topographic drag and reduce the flow in the channel to realistic values (Nadeau & Straub, 2009). The closures for subgrid-scale turbulence are standard and described in the Supplementary Information (Gent & McWilliams, 1990).

We use a linear equation of state with the same α and β values as the analytical model. The boundary conditions are free-slip at the bottom and no-slip along the side walls. A sea ice package is used to produce the required buoyancy flux over the channel (Jansen & Nadeau, 2016). The surface heat flux is computed from bulk formulas, as described in Jansen (2017) and in the Supporting Information, which are essentially a restoring boundary condition in sea-ice free regions. We prescribe the evaporation minus precipitation (E-P) as a freshwater flux given by:

$$E - P = E_0 f(y) \tag{8}$$

where $f(y)$ is a function of latitude with units of m s^{-1} and a magnitude corresponding to present day freshwater fluxes as shown in Figure 2b. The function $f(y)$ stays the same in all simulations while we vary the magnitude of the freshwater flux through E_0. $E_0 = 1$ corresponds approximately to the present-day zonally-averaged E-P values as diagnosed from the ECCO product (Forget et al., 2015). We apply a zonal wind stress only over the latitudes of the southern channel, which is imposed as an atmospheric zonal wind from which the EXF package (Large & Pond, 2002) computes the surface stress (Figure 2c).

We report results from experiments with the two different basin widths. All experiments start with $E_0 = 0$ and are run to equilibrium for 17,000 years, then E_0 is increased smoothly at a rate of 0.05 E_0 every 4,000 years. Since the freshwater flux is changed so slowly, the simulations are in quasi-steady state for almost all times. We kept increas-

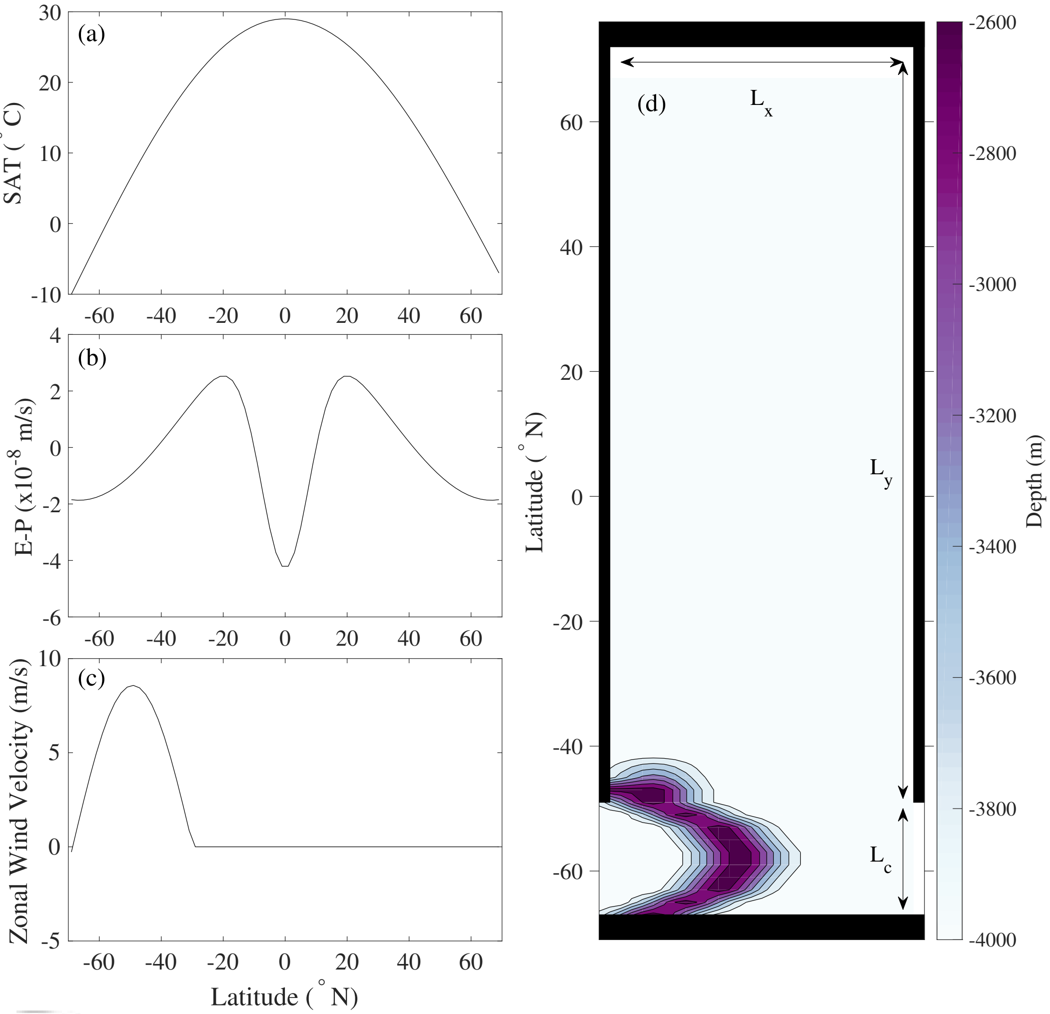

Figure 2. Surface forcing and geometry for the primitive equation model. All forcing functions vary only in latitude and not in longitude. (a) The prescribed surface air temperature used to compute air-sea heat fluxes. (b) The reference freshwater flux (E-P, evaporation - precipitation) for $E_0 = 1$ in equation (8). The magnitude of the freshwater flux is varied across simulations by changing the value of E_0. (c) A wind stress over the southern re-entrant channel is computed from the zonal wind. (d) The model geometry. We run experiments with two widths (L_x), a narrow Atlantic-like basin, and a wide Pacific-like basin. We included a Scotia Arc-like topographic feature in the channel.

ing E_0 until convection shut off in the northern hemisphere. All diagnostics are computed from averages over the last 1,000 simulation years.

3.2 Results

Based on the two-layer model analysis, we anticipate a stronger salinity gradient in the wider basin than in the narrow basin. Fig. 3b,c shows that while the surface salinity patterns are similar in the narrow and wide basins, the depth-averaged salinity difference between low and high latitudes is much larger in the wider basin for the same freshwater forcing (Fig. 3a). The increase in salinity gradient is not strictly monotonic for the narrow basin due to self-sustained oscillations that develop in the overturning strength at values of E_0 just above 1. A similar finding is discussed in Wolfe and Cessi (2015).

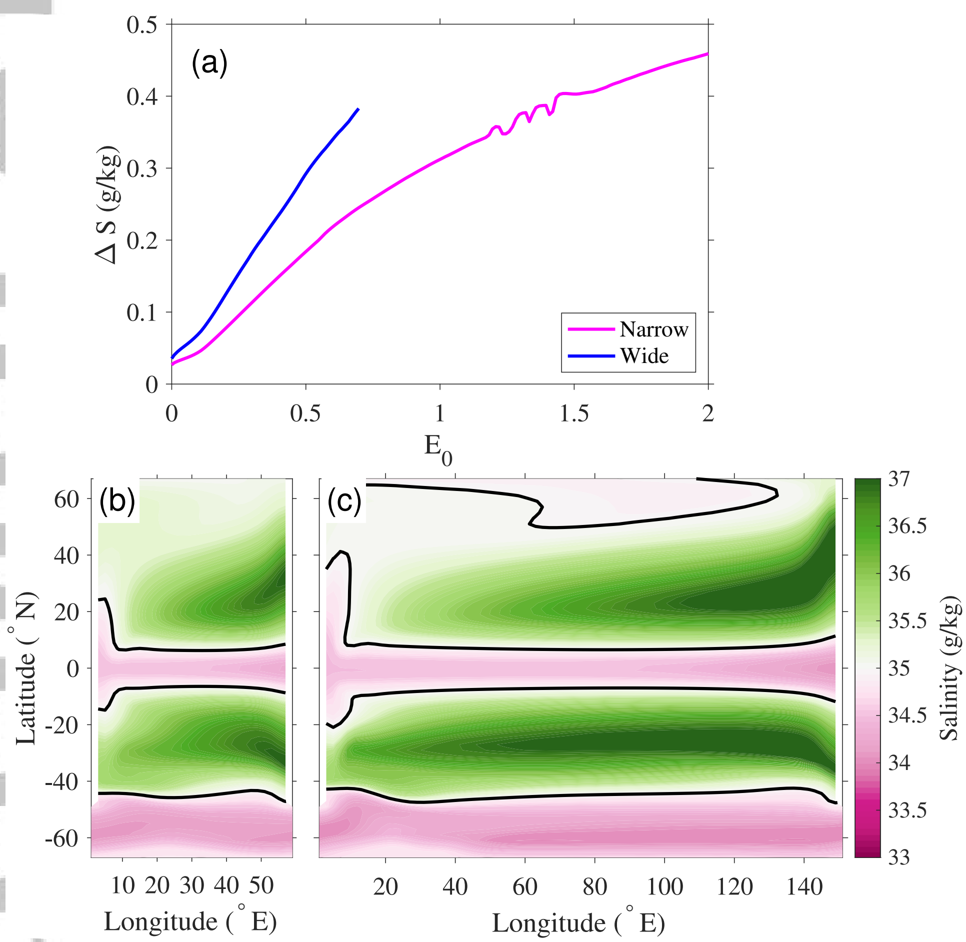

Figure 3. The wider basin shows a stronger salinity gradient in the MITgcm simulations. Panel (a) shows the difference in salinity between the northern boundary and 27 degrees north depth-averaged salinity for the narrow and wide basin simulations. The lines stop for the E_{0crit} at which convection shuts off. Panels (b) and (c) show the the surface salinity in the narrow (b) and wide (c) basins for a simulation run with $E_0 = 0.5$.

Fig. 4a shows the strength of the overturning circulation versus E_0 quantified as the zonally-averaged maximum stream function at the northern-most grid box. The overturning shuts off in the wide basin at a lower E_{0crit} where $E_{0crit} \simeq 0.65$ than in the narrow basin where $E_{0crit} \simeq 2$. Only the narrow basin convects at the "present day" freshwater forcing. The overturning is approximately twice as strong in the wide basin compared to the narrow basin, even though the wider basin is 2.6 times wider. This is consistent with the analytical model prediction that the difference in E_{0crit} stems from the fact that ψ_n and the freshwater flux integrated over the whole basin scale differently with basin width.

Somewhat surprisingly the overturning strength does not decrease monotonically for increasing E_0 as predicted by the analytical model. In the narrow basin simulations the overturning slightly increases with E_0, while in the wide basin ones changes are small and non monotonic. The behavior is driven by increases in the adiabatic upwelling in the southern channel ψ_s through physics we ignored in the analytical model. As can be seen in Fig. 3a, the salinity gradient increases more rapidly in the southern than in the northern hemisphere for increasing E_0, especially in the narrow basin, because buoyancy-driven gyres develop in the northern hemisphere (but not in the channel which has no lateral walls) which contribute additional salt transport to high latitudes. This asymmetry reduces the buoyancy gradient across the southern channel compared to the northern hemisphere. As a result the dense waters of the deep layer outcrop further south in the channel and thus the isopycnal slope decreases. A reduction in isopycnal slope h/ℓ is associated with an increase in ψ_s as predicted by the analytical scaling in Eq. (3). While the analytical model could be extended to include these effects by explicitly adding an equation for ℓ, such embellishments would not affect the key result that ψ_u and ψ_s have a different dependence on basin size than ψ_n. It is this difference that results in the dependence of E_{0crit} on basin size.

The numerical model has a somewhat different bifurcation: it is more like a supercritical bifurcation (Fig. 4a). The full model has more flexibility in adjusting the stratification and the southern channel; nevertheless, it shows the same rapid shutdown and the non-existence of a strong ψ above E_{0crit}.

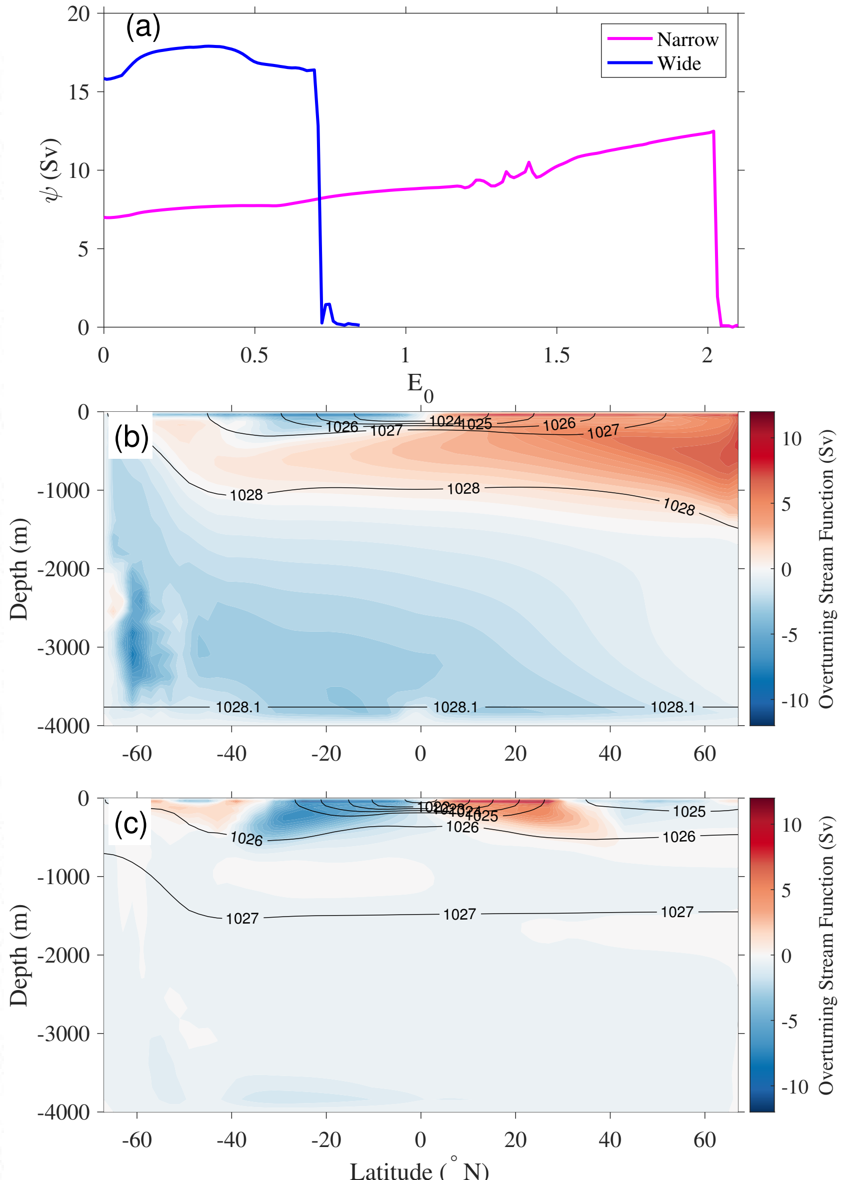

Figure 4. MITgcm simulations show that convection shuts off for a lower freshwater forcing E_{0crit} in the wider basin. Panel (a) shows overturning versus freshwater forcing for the narrow and wide basin. Panels (b,c) show overturning in the narrow basin before (b) and after convection shut off (c).

4 Discussion and Conclusions

An extension of the two-layer analytical model developed by Gnanadesikan (1999) was used to compute the critical freshwater forcing at which high latitude convection shuts-off in a single-basin ocean connected to a re-entrant channel. We found that the wider the basin, the smaller the value of the critical freshwater forcing (Fig. 5). The dependence on basin size arises because the salinity difference between low and high latitudes, which counteracts the temperature difference's effect on density and thus suppresses high latitude convection, is higher in a wider basin. The salinity difference is set by the ratio of the freshwater flux into the ocean, which observations suggest is approximately constant per unit area (Forget et al., 2015), and inversely proportional to the overturning streamfunction, which established scalings show that it is larger per unit area in a narrower basin. Idealized single-basin simulations agree with the analytical model predictions that convection shuts off for weaker freshwater forcing in a wider basin. For present day freshwater forcing, our theory correctly predicts that convection is suppressed in a basin as wide as the North Pacific, but not in a basin as wide as the North Atlantic.

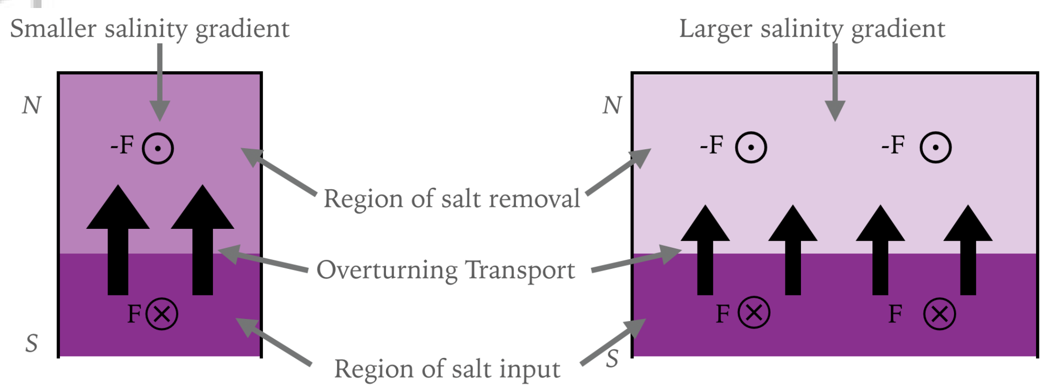

Figure 5. With a wider basin, the overturning is weaker per unit width, but the freshwater fluxes are the same per unit width, leading to a larger salinity gradient and a fresher northern part of the basin. This leads to a less dense convection region, and convection shut-off with weaker freshwater forcing.

Many plausible arguments have been advanced for why convection is observed only in the North Atlantic (Ferreira et al., 2018, and references therein). Our work finds that scalings for the meridional overturning circulation favors convection in a smaller basin. In the ocean all these mechanisms are likely to be at play and their relative importance may differ in varied climates and continental configurations. By providing scaling laws for each contribution, we are in a better position to quantify each one and determine which is most important in any specific climate.

Future work will consider more realistic simulations of the ocean circulation and quantify the relative importance of the various mechanisms that favors convection in the North Atlantic. It is also possible that the mechanisms are not independent of each other and the interactions could play an important role in past climate transitions and future climate changes. Our work should not be taken as a theory for why deep convection is observed in the North Atlantic but not in the North Pacific. Rather we contribute new insight to this fundamental climate question. It seems that two fluid layers, a salt budget, and well established overturning scalings are all that is required to demonstrate the importance of basin width on high-latitude convection.

Acknowledgments

MKY and RF acknowledge support through NSF awards OCE-1536515 and AGS-1835576. MKY acknowledges funding from National Defense Science and Engineering Graduate Fellowship and the American Meteorological Society Graduate Student Fellowship. GRF was supported by NSF OCE-1459702. The MITgcm code to run the model is found at `https://doi.org/10.5281/zenodo.3875142`.

References

Boyle, E. A. (1990). Quaternary deepwater paleoceanography. *Science*, *249*(4971), 863.

de Boer, A., & Hogg, A. M. (2014). Control of the glacial carbon budget by topographically induced mixing. *Geophysical Research Letters*.

Dijkstra, H. A. (2007). Characterization of the multiple equilibria regime in a global ocean model. *Tellus A*, *59*(5), 695–705.

Ferrari, R., Nadeau, L.-P., Marshall, D. P., Allison, L. C., & Johnson, H. L. (2017). A model of the ocean overturning circulation with two closed basins and a reentrant channel. *Journal of Physical Oceanography*, *47*(12), 2887–2906.

Ferreira, D., Cessi, P., Coxall, H. K., de Boer, A., Dijkstra, H. A., Drijfhout, S. S., … Wills, R. C. (2018, may). Atlantic-Pacific Asymmetry in Deep Water Formation. *Annual Review of Earth and Planetary Sciences*, *46*(1), 327–352. doi: 10.1146/annurev-earth-082517-010045

Ferreira, D., Marshall, J., & Campin, J.-M. (2010). Localization of deep water formation: Role of atmospheric moisture transport and geometrical constraints on ocean circulation. *Journal of Climate*, *23*(6), 1456–1476.

Forget, G., Campin, J.-M., Heimbach, P., Hill, C., Ponte, R., & Wunsch, C. (2015). ECCO version 4: an integrated framework for non-linear inverse modeling and global ocean state estimation.

Forget, G., & Ferreira, D. (2019). Global ocean heat transport dominated by heat export from the tropical pacific. *Nature Geoscience*, *12*(5), 351.

Gent, P. R., & McWilliams, J. C. (1990). Isopycnal mixing in ocean circulation models. *Journal of Physical Oceanography*, *20*(1), 150–155.

Gnanadesikan, A. (1999). A simple predictive model for the structure of the oceanic pycnocline. *Science*, *283*(5410), 2077–2079.

Gnanadesikan, A., Kelson, R., & Sten, M. (2018). Flux Correction and Overturning Stability: Insights from a Dynamical Box Model. *Journal of Climate*.

Haney, R. L. (1971). Surface thermal boundary condition for ocean circulation models. *Journal of Physical Oceanography*, *1*(4), 241–248.

Holmes, R. M., Zika, J. D., Ferrari, R., Thompson, A. F., Newsom, E. R., & England, M. H. (2019). Atlantic ocean heat transport enabled by indo-pacific heat uptake and mixing. *Geophysical Research Letters*.

Jansen, M. F. (2017). Glacial ocean circulation and stratification explained by reduced atmospheric temperature. *Proceedings of the National Academy of Sciences*, *114*(1), 45–50.

Jansen, M. F., & Nadeau, L.-P. (2016). The Effect of Southern Ocean Surface Buoyancy Loss on the Deep-Ocean Circulation and Stratification. *Journal of Physical Oceanography*, *46*(11), 3455–3470.

Johnson, H. L., Marshall, D. P., & Sproson, D. A. (2007). Reconciling theories of a mechanically driven meridional overturning circulation with thermohaline forcing and multiple equilibria. *Climate Dynamics*, *29*(7-8), 821–836.

Jones, C. S., & Cessi, P. (2016). Interbasin transport of the meridional overturning circulation. *Journal of Physical Oceanography*, *46*(4), 1157–1169.

Jones, C. S., & Cessi, P. (2017). Size Matters: Another Reason Why the Atlantic Is Saltier than the Pacific. *Journal of Physical Oceanography*, *47*(11), 2843–2859. doi: 10.1175/jpo-d-17-0075.1

Large, W. G., & Pond, S. (2002). Open Ocean Momentum Flux Measurements in Moderate to Strong Winds. *Journal of Physical Oceanography*, *11*(3), 324–336.

doi: 10.1175/1520-0485(1981)011⟨0324:oomfmi⟩2.0.co;2

Loving, J. L., & Vallis, G. K. (2005). Mechanisms for climate variability during glacial and interglacial periods. *Paleoceanography*, *20*(4).

Marotzke, J., Welander, P., & Willebrand, J. (1988). Instability and multiple steady states in a meridional-plane model of the thermohaline circulation. *Tellus A: Dynamic Meteorology and Oceanography*, *40*(2), 162–172.

Marshall, D. (1997). Subduction of water masses in an eddying ocean. *Journal of Marine Research*, *55*(2), 201–222.

Marshall, J., Adcroft, A., Hill, C., Perelman, L., & Heisey, C. (1997). A finite-volume, incompressible Navier Stokes model for studies of the ocean on parallel computers. *Journal of Geophysical Research: Oceans*, *102*(C3), 5753–5766.

Marshall, J., & Radko, T. (2003). Residual-mean solutions for the Antarctic Circumpolar Current and its associated overturning circulation. *Journal of Physical Oceanography*, *33*(11), 2341–2354.

Munk, W. H. (1966). Abyssal recipes. In *Deep sea research and oceanographic abstracts* (Vol. 13, pp. 707–730).

Nadeau, L.-P., & Straub, D. N. (2009). Basin and Channel Contributions to a Model Antarctic Circumpolar Current. *Journal of Physical Oceanography*, *39*(4), 986–1002. doi: 10.1175/2008jpo4023.1

Newsom, E. R., & Thompson, A. F. (2018). Reassessing the role of the indo-pacific in the ocean's global overturning circulation. *Geophysical Research Letters*, *45*(22), 12–422.

Nikurashin, M., & Vallis, G. (2011). A theory of deep stratification and overturning circulation in the ocean. *Journal of Physical Oceanography*, *41*(3), 485–502.

Nikurashin, M., & Vallis, G. (2012). A theory of the interhemispheric meridional overturning circulation and associated stratification. *Journal of Physical Oceanography*, *42*(10), 1652–1667.

Nilsson, J., Langen, P. L., Ferreira, D., & Marshall, J. (2013). Ocean basin geometry and the salinification of the atlantic ocean. *Journal of Climate*, *26*(16), 6163–6184. Retrieved from `https://journals.ametsoc.org/doi/pdf/10.1175/JCLI-D-12-00358.1` doi: 10.1175/JCLI-D-12-00358.1

Rahmstorf, S. (1996). On the freshwater forcing and transport of the Atlantic thermohaline circulation. *Climate Dynamics*, *12*(12), 799–811.

Rahmstorf, S., Box, J. E., Feulner, G., Mann, M. E., Robinson, A., Rutherford, S., & Schaffernicht, E. J. (2015). Exceptional twentieth-century slowdown in Atlantic Ocean overturning circulation. *Nature climate change*, *5*(5), 475.

Sgubin, G., Swingedouw, D., Drijfhout, S., Mary, Y., & Bennabi, A. (2017). Abrupt cooling over the North Atlantic in modern climate models. *Nature communications*, *8*, 14375.

Shakespeare, C., & Hogg, A. M. (2012). An Analytical Model of the Response of the Meridional Overturning Circulation to Changes in Wind and Buoyancy Forcing. *Journal of Physical Oceanography*.

Stommel, H. (1961). Thermohaline convection with two stable regimes of flow. *Tellus*, *13*(2), 224–230.

Thornalley, D. J., Barker, S., Broecker, W. S., Elderfield, H., & McCave, I. N. (2011). The deglacial evolution of North Atlantic deep convection. *Science*, *331*(6014), 202–205.

Timmermann, A., Gildor, H., Schulz, M., & Tziperman, E. (2003). Coherent resonant millennial-scale climate oscillations triggered by massive meltwater pulses. *Journal of Climate*, *16*(15), 2569–2585.

Walin, G. (1985). The thermohaline circulation and the control of ice ages. *Palaeogeography, palaeoclimatology, palaeoecology*, *50*(2-3), 323–332.

Weijer, W., de Ruijter, W. P., Dijkstra, H. A., & Van Leeuwen, P. J. (1999). Impact of interbasin exchange on the atlantic overturning circulation. *Journal of Physical Oceanography*, *29*(9), 2266–2284.

Wolfe, C. L., & Cessi, P. (2015). Multiple regimes and low-frequency variability in the quasi-adiabatic overturning circulation. *Journal of Physical Oceanography*, *45*(6), 1690–1708.

Figure 1.

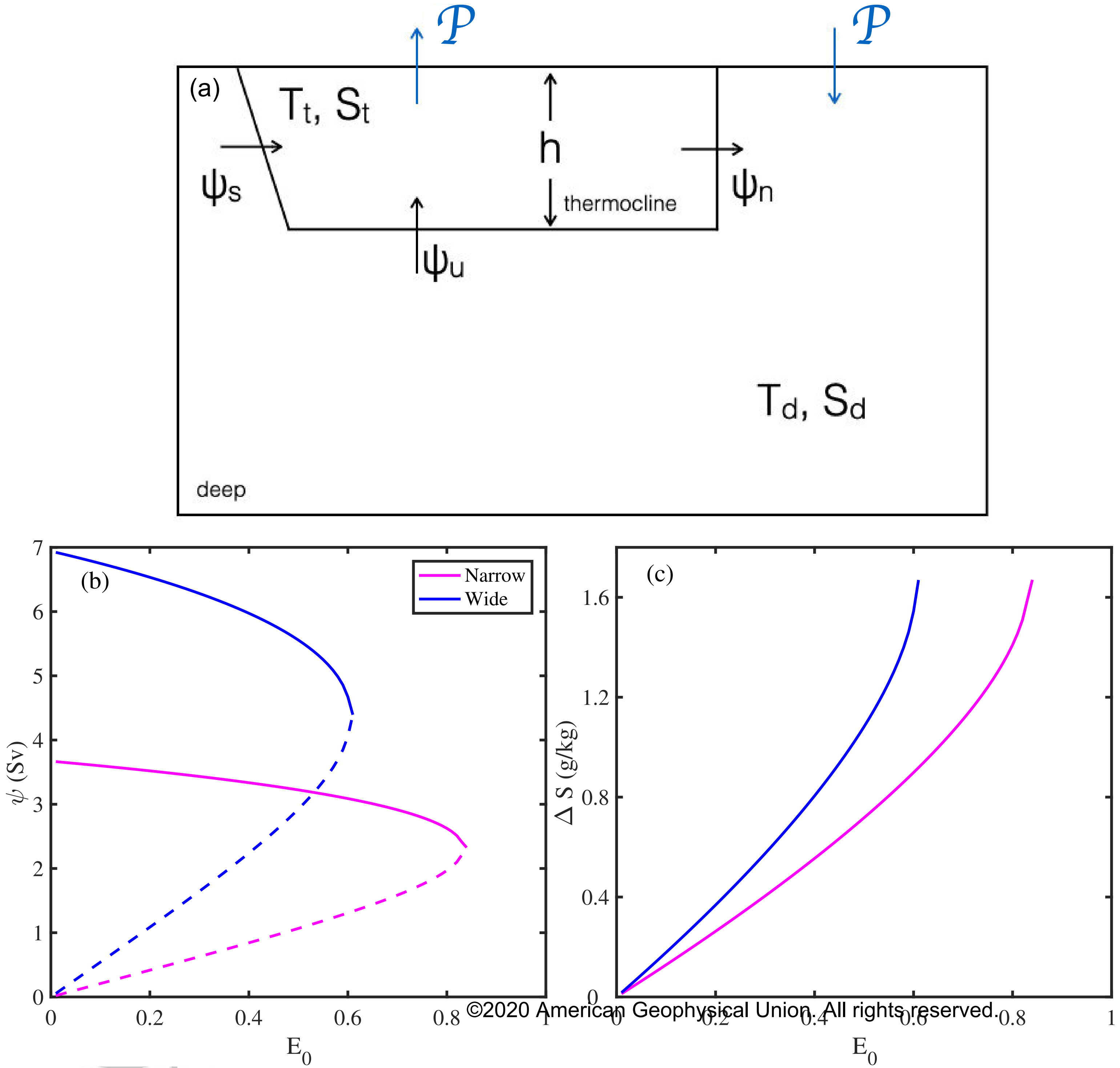
(a)
$\mathcal{P}$
$\mathcal{P}$
T_t, S_t
h
ψ_s
ψ_n
thermocline
ψ_u
T_d, S_d
deep
(b)
Narrow
Wide
ψ (Sv)
E_0
(c)
Δ S (g/kg)
E_0

Figure 2.

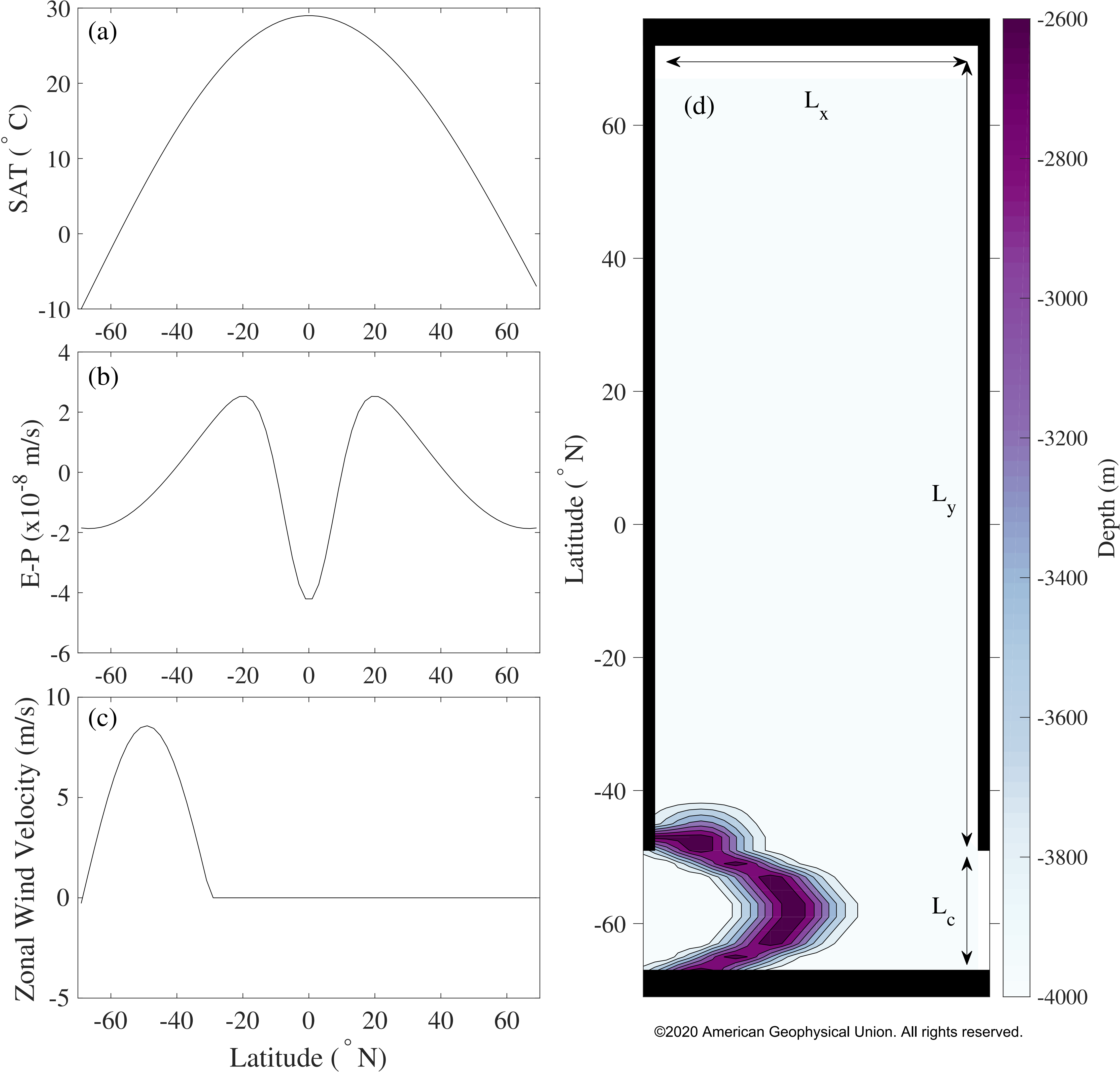
(a)
SAT (°C)
30
20
10
0
-10
-60
-40
-20
0
20
40
60
(b)
E-P (x10^-8 m/s)
4
2
0
-2
-4
-6
(c)
Zonal Wind Velocity (m/s)
10
5
0
-5
Latitude (°N)
(d)
L_x
L_y
L_c
Latitude (°N)
Depth (m)
-2600
-2800
-3000
-3200
-3400
-3600
-3800
-4000

Figure 3.

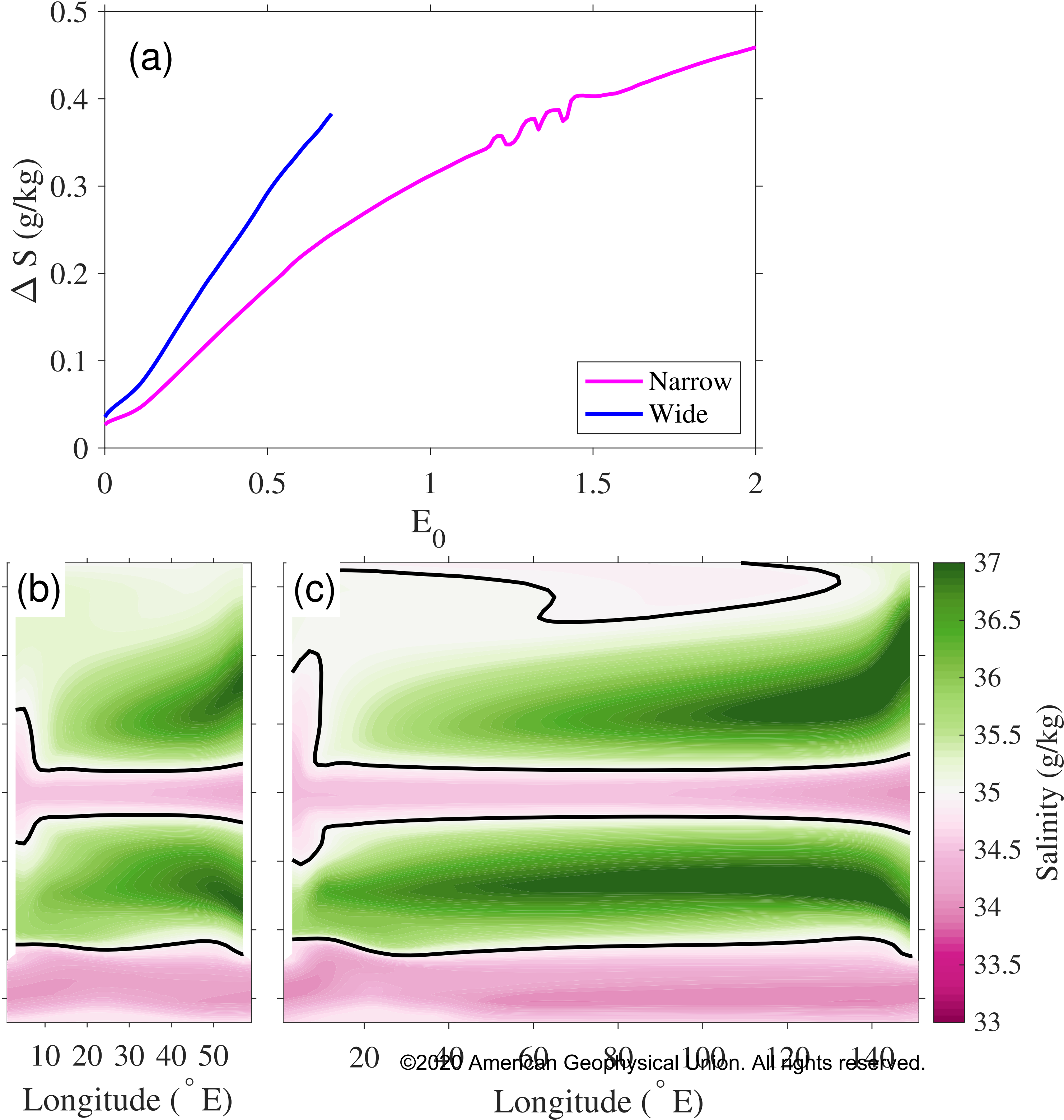

(a)
0.5
0.4
0.3
0.2
0.1
0
Δ S (g/kg)
Narrow
Wide
0
0.5
1
1.5
2
E_0
(b)
(c)
60
40
20
0
-20
-40
-60
Latitude (° N)
10 20 30 40 50
Longitude (° E)
20 40 60 80 100 120 140
Longitude (° E)
37
36.5
36
35.5
35
34.5
34
33.5
33
Salinity (g/kg)

Figure 4.

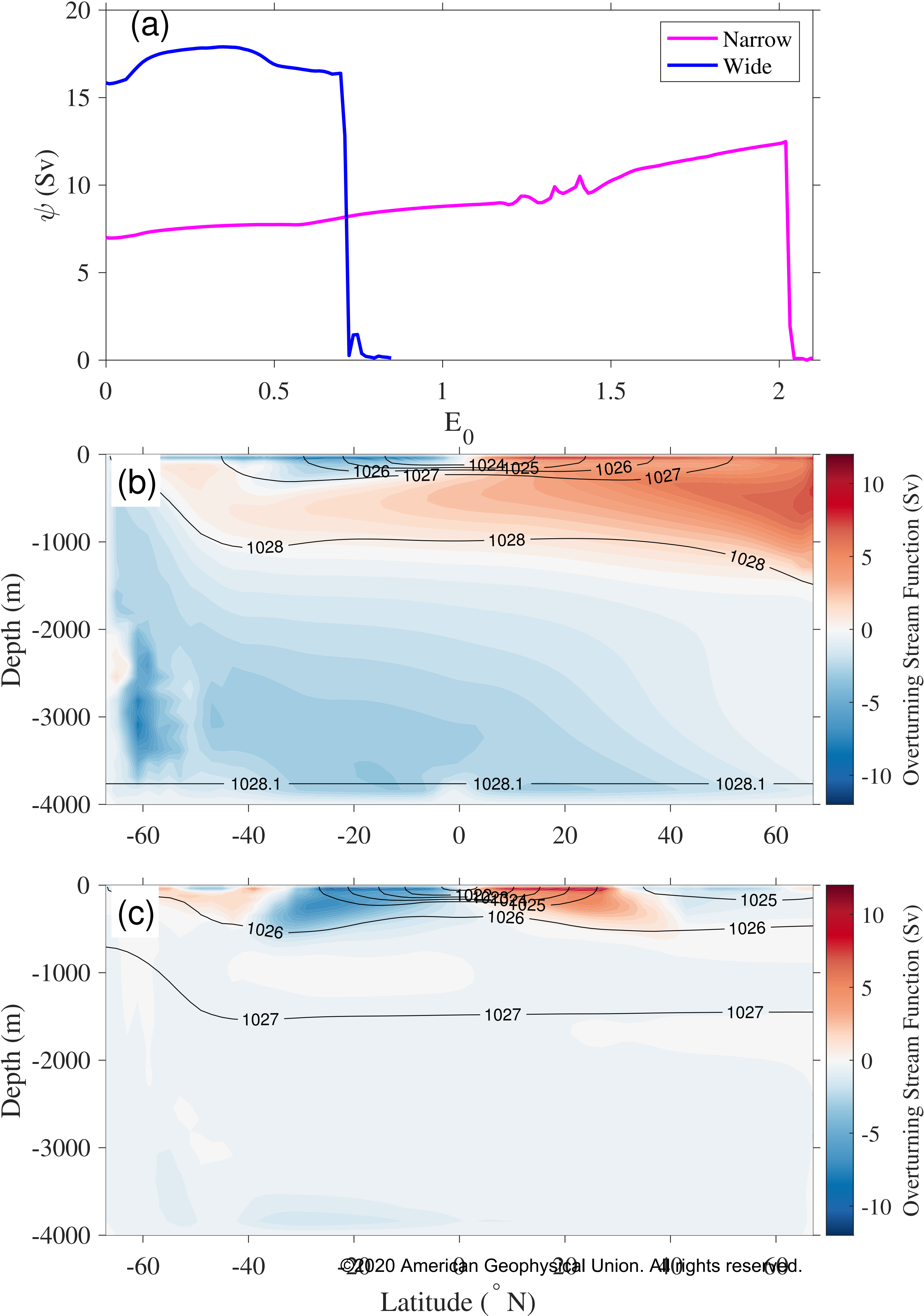
(a)
Narrow
Wide
ψ (Sv)
E0
(b)
(c)
Depth (m)
Overturning Stream Function (Sv)
Latitude (° N)
1024
1025
1026
1027
1028
1028.1

Figure 5.

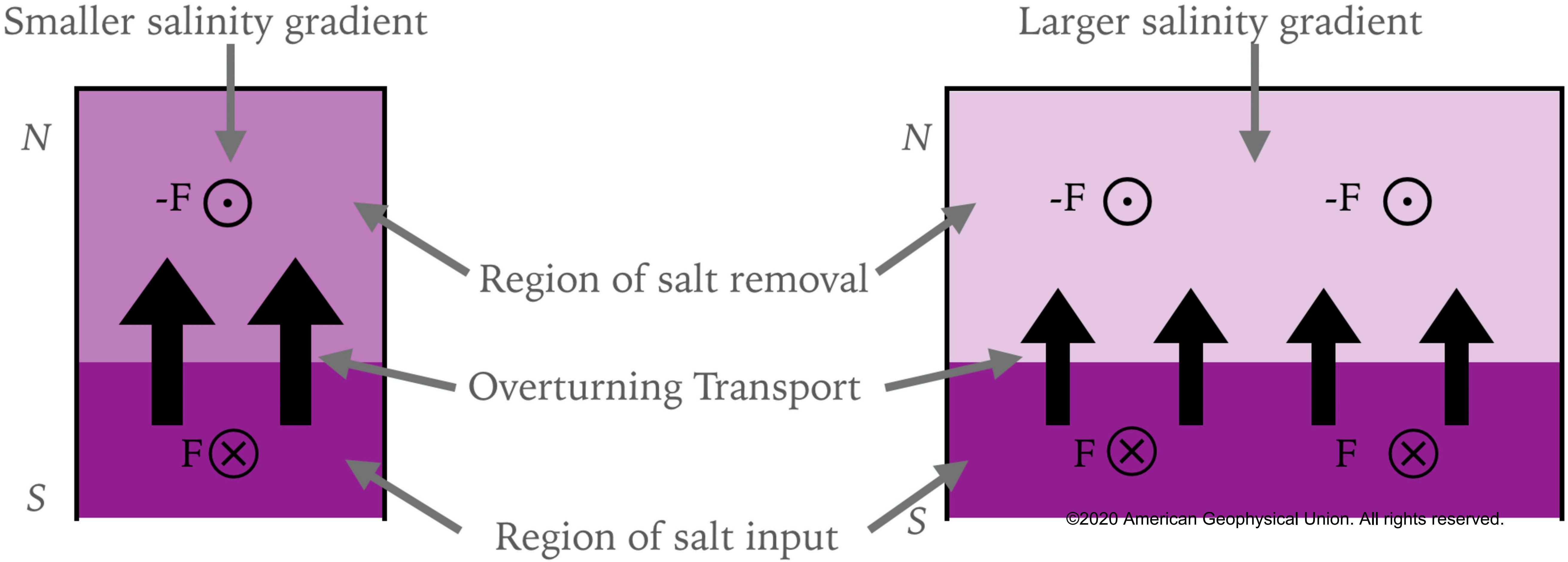
Smaller salinity gradient
Larger salinity gradient
N
-F
-F
-F
Region of salt removal
Overturning Transport
F
F
F
S
Region of salt input
S
N